Chinese Chemical Letters 35 (2024) 109050

Contents lists available at ScienceDirect

Chinese Chemical Letters

journal homepage: www.elsevier.com/locate/cclet

Computational design of bimetallic TM_2@g-C_9N_4 electrocatalysts for enhanced CO reduction toward C_2 products

Jiajun Wang[a], Guolin Yi[a], Shengling Guo[a], Jianing Wang[b], Shujuan Li[c,*], Ke Xu[c], Weiyi Wang[b,*], Shulai Lei[c,d,*]

[a] Tianjin Key Laboratory of Structure and Performance for Functional Molecules, College of Chemistry, Tianjin Normal University, Tianjin 300387, China
[b] Department of Chemical Physics & Hefei National Laboratory for Physical Sciences at Microscale, University of Science and Technology of China, Hefei 230026, China
[c] Hubei Key Laboratory of Low Dimensional Optoelectronic Materials and Devices, Hubei University of Arts and Science, Xiangyang 441053, China
[d] Hubei Longzhong Laboratory, Xiangyang 441053, China

ARTICLE INFO

Article history:
Received 30 June 2023
Revised 11 August 2023
Accepted 3 September 2023
Available online 5 September 2023

keywords:
C_9N_4 monolayer
Double-atom catalysts
CO electroreduction
Multi-carbon products
Density functional theory

ABSTRACT

Electrochemical CO reduction (ECOR) as a potential strategy for producing valuable chemicals and fuels has captured substantial attention. However, the currently available electrocatalysts suffer from poor selectivity and low Faradaic efficiency, limiting their industrial application. Herein, we systematically investigate the potential of homonuclear bimetallic electrocatalysts, TM_2@C_9N_4 (TM = Fe, Co, Ni, and Cu), for the ECOR through extensive density functional theory calculations. Our findings suggest that all four proposed monolayers exhibit exceptional stability, making them highly suitable for experimental synthesis and practical applications. Interestingly, these transition-metal dual atoms anchored on C_9N_4 monolayers show great potential in facilitating the production of high-value C_2 products, such as C_2H_5OH and C_2H_4, due to the significantly low limiting potentials (-0.06∼-0.46 V) and small kinetic energy barriers (0.54–1.08 eV) for the CO coupling process. Moreover, with the exception of Ni_2@C_9N_4, these bimetallic catalysts demonstrate the impressive suppression of the competitive hydrogen evolution reaction (HER), leading to a high selectivity for C_2 products in ECOR. Our predictions would accelerate the development of high-performance C_9N_4-based dual-atom catalysts for the ECOR.

As a significant topic in the energy field, electrochemical CO_2 reduction (ECO_2R) has emerged as a promising strategy for reducing carbon emissions and building carbon-neutral energy infrastructures [1–3]. In spite of the great potential advantages, effective electrocatalysts for direct conversion of CO_2 to more value-added multi-carbon products (*e.g.*, ethylene, ethane, ethanol, and 1-propanol) remain elusive due to the high overpotential and low productivity [4]. By contrast, the technologies of ECO_2R to CO have been well developed, and a wealth of electrocatalysts can achieve a Faradaic efficiency (FE) larger than 90% [5]. In this regard, there is a growing demand for further advancing the electrochemical CO reduction (ECOR) performance towards desired multi-carbon products [6–12]. Consequently, the design of an efficient ECOR catalyst with high activity, excellent stability, and eminent selectivity is of paramount importance and greatly demanded.

Recently, single-atom catalysts (SACs) featuring isolated atom active sites dispersed on substrates have been developed as promising candidates for the ECOR due to the ultimate atom utilization efficiency and desirable electronic states [13–17]. However, because SACs usually have strong linear scaling relationships between the adsorption strength of reaction intermediates, they still face many challenges in simultaneously enhancing the productivity and FE of the ECOR [18]. Furthermore, it is commonly accepted that effective coadsorption of multiple CO and active CO coupling are of great importance for achieving the production of multi-carbon products [19–21]. On the basis of those considerations, the construction of double-atom catalysts (DACs) by loading two atoms onto the substrate provides a new avenue for the ECOR, which not only retains the advantages of SACs but can also have synergetic interatomic interactions and more active centers. For example, Li *et al.* [22] synthesized a dual Cu-Cu atomic catalyst, which exhibited an outstanding ECOR activity for C_{2+} products, with FE of 91% and current density > 90 mA/cm^2. Rong *et al.* [23] showed that few Cu atoms anchored on graphdiyne can efficiently catalyze CO reduction to acetate with an unprecedentedly high FE of

* Corresponding authors.
E-mail addresses: 11724@hbuas.edu.cn (S. Li), dancingw@ustc.edu.cn (W. Wang), sllei@hbuas.edu.cn (S. Lei).

https://doi.org/10.1016/j.cclet.2023.109050
1001-8417/

53.8%. Through density functional theory (DFT) calculations, a series of DACs, such as Cu+B@g-C_3N_4, Cu_2@g-C_6N_6, TM+B@BlackP, B+P@C_2N [24–29], have been theoretically designed, which have low limiting potentials and small CO coupling barriers for generating multi-carbon products. However, it remains a great challenge to readily and rationally construct DACs with high catalytic performance toward the ECOR.

In recent years, various novel two-dimensional (2D) carbon-nitrogen systems, including g-C_3N_4, C_2N and g-C_6N_6, have garnered significant attention in numerous fields of energy catalysis owing to the large surface area, high stability, and rich coordination environment [30–34]. As a member of the carbon-nitrogen family, C_9N_4 monolayer possesses several desirable characteristics, such as high thermal and dynamical stability, nodal-line semimetallic property, and periodic nanopores, which is conducive to single/dual-atom catalysis [35]. For instance, Zhou *et al.* [36] theoretically found that C_9N_4 monolayer anchored with a single Ni atom could perform as a promising water-splitting electrocatalyst with N and Ni atoms as catalytic active sites for the hydrogen evolution reaction (HER) and oxygen evolution reaction (OER), respectively. Xue *et al.* [37] conducted high-throughput calculations on TM@C_9N_4 to screen the potential nitrogen reduction reaction (NRR) catalysts, and discovered that W@C_9N_4 exhibited the best catalytic activity with the limiting potential of −0.24 V. He *et al.* [38] reported the B-doped C_9N_4 monolayer possessed good catalytic performance for the oxygen reduction reaction (ORR) with an overpotential of 0.98 V. Sun *et al.* [39] systematically investigated the NRR performance of dual-metal TM_1TM_2@C_9N_4 electrocatalysts, and obtained five high activity catalysts with favorable limiting potentials of −0.33 V to −0.53 V. However, to the best of our knowledge, there have been no reports of the ECOR on C_9N_4 based bimetallic electrocatalysts.

Hence, in this work, we perform the first-principles theoretical calculations to systematically explore the potential of C_9N_4 monolayers anchored with four types of transition metal dual atoms (TM_2@C_9N_4; TM = Fe, Co, Ni, and Cu) as the ECOR electrocatalysts because of the high catalytic activity and cost-effectiveness. We firstly examine the structural stabilities, CO adsorption abilities and CO coupling process of the TM_2@C_9N_4 systems, and then calculate their free energy diagrams for the ECOR toward C_1 and C_2 products. According to the computed limiting potentials (−0.06∼−0.46 V) and kinetic energy barriers for the CO coupling process (0.54–1.08 eV), our designed systems except for Ni_2@C_9N_4 are confirmed to have good catalytic activities and high selectivity toward C_2 products, compared with the competing C_1 products and HER. These findings demonstrate that the bimetallic TM_2@C_9N_4 systems can act as high-performance catalysts for electrochemical reducing CO to value-added multi-carbon products.

The spin-polarized DFT calculations in this study are performed using the Vienna *ab initio* Simulation Package (VASP) [40]. The electron-ion interactions are described using the projected augmented plane wave (PAW) method [41], and the exchange-correlation energies are calculated using the generalized gradient approximation theory proposed by Perdew, Burke, and Ernzerhof (GGA-PBE) [42]. Moreover, the van der Waals weak interaction between the adsorbates and substrate is further treated using Grimme's semiempirical correction scheme (DFT-D3) method [43]. In all our calculations, the plane wave cutoff energy is set to 500 eV A vacuum layer of 20.0 Å is introduced along the z-direction to minimize the interaction between two periodic units. The structure optimization and electronic property calculations are performed using Γ-centered 2 × 2 × 1 and 4 × 4 × 1 k-point grids according to the Monkhorst-Pack scheme [44]. The convergence criteria for the total energy and maximum force per atom are set as 10^{-5} eV and 0.02 eV/Å, respectively. To obtain the transition states and kinetic barriers for the CO coupling reaction, the climbing-image nudged elastic band (CI-NEB) method is employed [45]. More computational details about the binding energy and ECOR are given in the Supporting information.

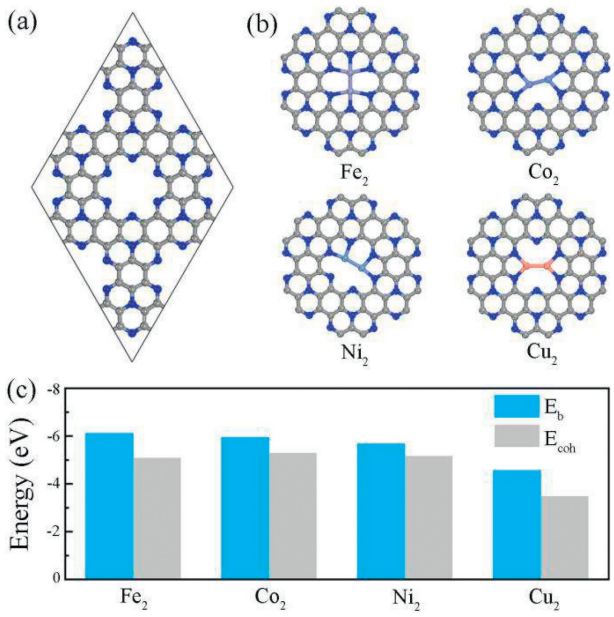

Fig. 1. Optimized geometrical structure of (a) pristine C_9N_4 monolayer and (b) the most stable TM_2@C_9N_4 systems. (c) Computed binding energies of the considered double TM atoms anchored on C_9N_4 monolayer. Here, the cohesive energies of corresponding bulk material are also given for comparison.

Firstly, the geometric structures and stabilities of the proposed TM_2@C_9N_4 monolayers are investigated. We construct a 2 × 2 × 1 C_9N_4 supercell consisting of 72 carbon atoms and 32 nitrogen atoms (Fig. 1a). After the structural optimization using GGA-PBE, the calculated lattice constants ($a = b = 19.28$ Å), C–C bond lengths ($d_{C\text{-}C} = 1.42$ and 1.46 Å), and C–N bond lengths ($d_{C\text{-}N} = 1.34$ and 1.39 Å) are found to be consistent with previous reports [46–48]. The pristine C_9N_4 monolayer has an intrinsic central cavity surrounded by six sp^2 hybridized nitrogen atoms, with a diameter of approximately 5.52 Å Similar to the cases of g-C_3N_4 and C_2N, these nitrogen atoms with lone pair electrons also provide suitable coordination sites to anchor single or dual atoms. Hence, four typical transition metals, including Fe, Co, Ni, and Cu, are taken into consideration for constructing DACs. The most stable configurations for each bimetallic atoms are determined by comparing the calculated total energies, and are given in Fig. 1b. Clearly, there exist three types of anchoring sites: (1) S1 configuration, such as Fe_2@C_9N_4, in which two Fe atoms are bound to three adjacent N atoms with $d_{Fe\text{-}Fe} = 2.01$ Å, $d_{Fe\text{-}N} = 1.92$ and 2.21 Å; (2) S2 configuration, such as Cu_2@C_9N_4, in which each Cu atom is only bound to two nearest N atoms with $d_{Cu\text{-}Cu} = 2.25$ Å and $d_{Cu\text{-}N} = 1.91$ Å; (3) S3 configuration, in which two metal atoms are bound to two adjacent N atoms, but the two TM-N bond lengths are not equal, such as Co_2@C_9N_4 ($d_{Co\text{-}Co} = 2.09$ Å, $d_{Co\text{-}N} = 1.89$ and 2.02 Å) and Ni_2@C_9N_4 ($d_{Ni\text{-}Ni} = 2.16$ Å, $d_{Ni\text{-}N} = 1.84$ and 1.92 Å).

To verify the stability of TM_2@C_9N_4 systems, we calculate the binding energies (E_b) of the Fe_2, Co_2, Ni_2, and Cu_2 dual atoms on C_9N_4 monolayers, and compare them to the cohesive energies (E_{coh}) of the corresponding bulk material. As presented in Fig. 1c, the E_b values of these considered double TM atoms anchored on C_9N_4 monolayer range from −6.11 eV to −4.56 eV, close to those of other porous carbon nitride nanosheets anchored with dual metal atoms [49–52]. This is indicative of a strong interaction between the TM_2 dual atoms and C_9N_4 monolayer. It should be noted that due to the significantly increased surface free energy, the dual

metal atoms are peculiarly prone to aggregation of small clusters rather than being singly dispersed on supports during the reaction [53,54]. Fortunately, we can see that the E_b of all $TM_2@C_9N_4$ systems are more negative than the E_{coh} of respective bulk material, suggesting that the metal dual atoms tend to bind more strongly with the $TM_2@C_9N_4$ monolayers than with the metal bulk, thus potentially avoiding forming metal clusters. To gain further insight into the thermodynamic stabilities of $TM_2@C_9N_4$, we perform *ab initio* molecular dynamics (AIMD) simulations with a duration of 10 ps at 500 K. As presented in Fig. S1 (Supporting information), the total energies of these $TM_2@C_9N_4$ systems fluctuate within small ranges and no discernible damage to the geometrical structures occur after the 10 ps simulation. Moreover, the constructed DACs supported on C_9N_4 monolayers exhibit high durability, sustaining up to 500 K beyond common experimental conditions. These results indicate that our designed bimetallic $TM_2@C_9N_4$ systems have excellent stability and high feasibility in terms of various energy applications.

The electronic characteristics of electrocatalysts are of significant importance for the catalysis reaction. Thus, the band structures of $TM_2@C_9N_4$ systems are calculated and illustrated in Fig. S2 (Supporting information). We can see that all the proposed systems display metallic properties, which are favorable for facilitating electrocatalytic reactions. According to the charge density differences and Bader charge analysis (Fig. S3 in Supporting information), we find that the charge transfer from TM atoms to C_9N_4 monolayer with an amount of 1.46 |e| for $Fe_2@C_9N_4$, 1.30 |e| for $Co_2@C_9N_4$, 1.13 |e| for $Ni_2@C_9N_4$ and 1.14 |e| for $Cu_2@C_9N_4$, leaving the double TM atoms and C_9N_4 monolayers with positive and negative charges, respectively. In light of this, these metal dual atoms are in positive oxidation state, which would be conducive to the subsequent CO adsorption and activation. Overall, these facts ensure these proposed $TM_2@C_9N_4$ systems can act as potential ECOR electrocatalysts.

The initial step of catalytic reactions is typically driven by the adsorption of reactants, which can greatly influence or even dictate the following reaction mechanism. Thus, we then explore the adsorption performance of CO molecule, where three adsorption modes of (*e.g.*, O-end, C-end, and CO-side) in conjunction with various possible adsorption positions of $TM_2@C_9N_4$ are considered to obtain the most energetically stable adsorption structures. As illustrated in Fig. 2. we find that the bridging sites of double TM atoms exhibit strong affinity for CO molecule with the C-end configuration, forming TM-C bonds with the lengths of approximately 1.90, 1.88, 1.86, and 1.85 Å for TM = Fe, Co, Ni, and Cu, respectively. Notably, compared with the C–O bond length (1.13 Å) of a free CO molecule, the adsorbed CO molecules (*CO) have elongated bond lengths, *i.e.*, 1.19 Å for $Fe_2@C_9N_4$, 1.19 Å for $Co_2@C_9N_4$, 1.18 Å for $Ni_2@C_9N_4$, and 1.18 Å for $Cu_2@C_9N_4$. Furthermore, the adsorption energies (ΔE_{*CO}) of the CO molecules adsorbed on $TM_2@C_9N_4$ (TM = Fe, Co, Ni, and Cu) are calculated to be −2.03, −2.57, −2.12, and −2.42 eV, respectively. When considering the corrections of zero-point energy (ZPE) and entropy, the corresponding adsorption free energies (ΔG_{*CO}) of these *CO species are found to be −1.52, −2.02, −1.53, and −1.81 eV, respectively. These results demonstrate that our designed $TM_2@C_9N_4$ systems interact with the CO molecules through chemisorption, which are sufficiently strong to capture and activate the CO molecules.

Additionally, we further compute and analyze the projected density of states (PDOS) and charge density differences to understand the mechanism of CO activation. As shown in Fig. 2b, there are pronounced hybridization between the C-2p and TM-3d orbitals, indicating a strong coupling interaction. After CO adsorption, the magnetic moment of the Cu dual atoms is 0 μ_B, while the magnetic moments of the Fe, Co and Ni dual atoms are 3.80, 3.60 and 1.20 μ_B, respectively. As shown in Fig. S4 (Supporting information), the magnetic moments on the $Fe_2@C_9N_4$, $Co_2@C_9N_4$, and $Ni_2@C_9N_4$ systems can be attributed to the asymmetrical distributions of their respective 3d orbitals. Moreover, the charge density differences in Figs. 2c–f show that when the CO molecules are chemisorbed on the $TM_2@C_9N_4$ systems, electrons accumulate (yellow color) around the C and O atoms while deplete (cyan color) between the C–O bonds. It is indicative that the double TM atoms receive the lone-pair electron from the 5σ orbital of CO and simultaneously back-donate their electrons to the antibonding π^* orbital of CO, forming the accepting (σ)-donating (π) interaction. Bader charge analysis shows that 0.44 |e|, 0.38 |e|, 0.34 |e|, and 0.27 |e| are transferred to CO from the Fe_2, Co_2, Ni_2, and Cu_2 dual atoms, leading to the gathering of negative charges on the *CO species. These observed results rationalize the strong adsorption strength and sufficient activation of the CO molecules on $TM_2@C_9N_4$, which would be of benefit to the subsequent ECOR.

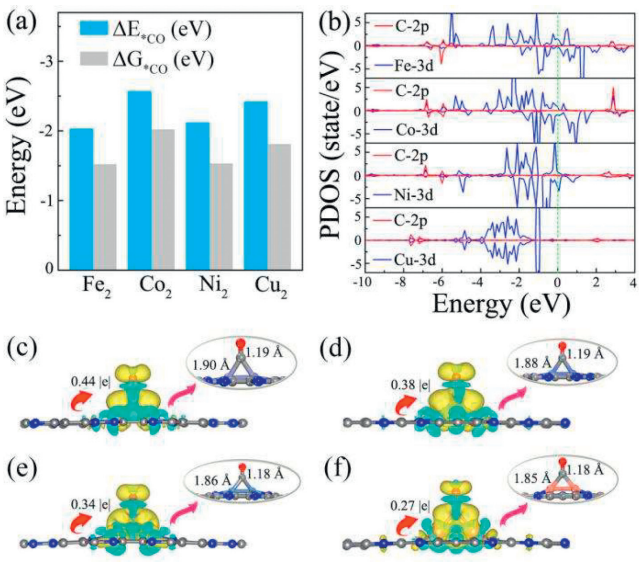

Fig. 2. (a) The computed adsorption energies, (b) projected density of states (PDOS) and (c-f) charge density differences with an isovalue of 0.003 e/Å^3 for the CO molecules on the designed $TM_2@C_9N_4$ systems, in which the charge depletion and accumulation are represented by the cyan and yellow colors, respectively. Insets show the optimized structures of CO adsorption.

After the thorough examination of the adsorption properties of CO molecules on the $TM_2@C_9N_4$ systems, we continue to investigate the subsequent ECOR toward various C_1 products. On the basis of the possible reaction paths for generating C_1 products shown in Fig. 3a, we explore the lowest-energy reaction paths for these $TM_2@C_9N_4$ catalysts, which are regarded as the ones with the least Gibbs free energy change (ΔG) between any two elementary reaction steps. The limiting potential (U_L), widely accepted index to assess the ECOR activity, is defined as the applied voltage required to make the whole reaction along the lowest-energy reaction path proceeds spontaneously. Consequently, we optimize the geometries of all ECOR intermediates in each elementary step and calculate their Gibbs free energies, which can be applied to establish the Gibbs free energy diagrams for the ECOR to C_1 products along the considered paths. According to the predicted free energy diagrams, the energetically most favorable reaction path and the corresponding U_L are clearly elucidated (Fig. 3 and Fig. S5 in Supporting information).

The results indicate that the ECOR process on the $Fe_2@C_9N_4$, $Co_2@C_9N_4$, and $Ni_2@C_9N_4$ catalysts prefer to proceed along the same $6e^-$ reduction pathway, in which CH_4 is identified as the final product. While for $Cu_2@C_9N_4$, it prefers to proceed *via* a $4e^-$ reduction pathway to form CH_3OH. The U_L values of respective

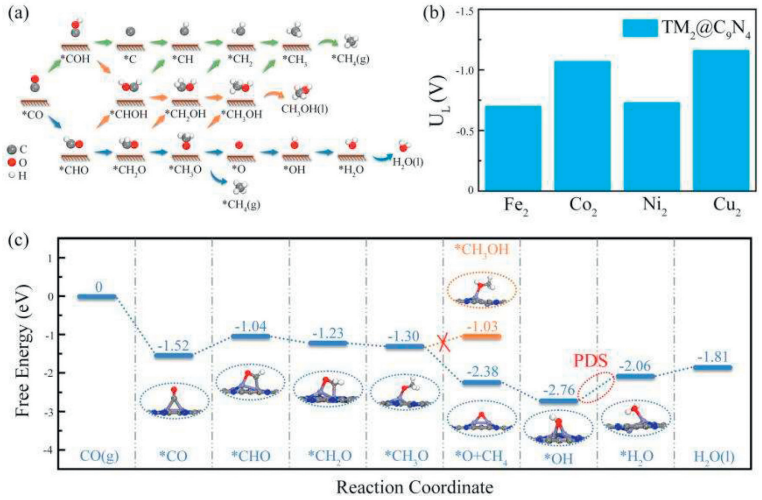

Fig. 3. (a) The possible reaction paths for the ECOR toward various C_1 products. (b) Computed limiting potentials of ECOR into C_1 products on the $TM_2@C_9N_4$ catalysts. (c) Gibbs free energy diagrams of ECOR into C_1 products on $Fe_2@C_9N_4$, in which the inset exhibits the corresponding geometric configurations of the intermediates in each elementary step.

most favorable reduction pathway are calculated to be −0.70 eV for $Fe_2@C_9N_4$, −1.07 eV for $Co_2@C_9N_4$, −0.73 eV for $Ni_2@C_9N_4$, and −1.16 eV for $Cu_2@C_9N_4$. Taking the $Fe_2@C_9N_4$ as a representative, the most favorable free energy profile for the ECOR to C_1 products is given in Fig. 3c for further clarification. One can see that the chemisorbed *CO is preferentially hydrogenated to generate the *CHO intermediate in the initial step, which is endothermic with the free energy rise of 0.48 eV Subsequently, the *CHO intermediate reacts with another two $(H^+ + e^-)$ pairs to produce the $*CH_3O$ intermediate, in which the Gibbs free energies fall by 0.19 and 0.07 eV, respectively. Furthermore, the fourth protonation step results in the dissociation of $*CH_3O$ into *O and CH_4. Remarkably, this CH_4-releasing step is exoergic with a negative ΔG value (−0.38 eV), which is lower than that of the formation of $*CH_3OH$ intermediate ($\Delta G = 0.27$ eV). After this, the remaining *O can be readily hydrogenated into *OH with a downhill free energy of 0.38 eV Finally, the hydrogenation of *OH to $*H_2O$ takes place after the sixth $(H^+ + e^-)$ pair attack, which requires an energy injection of 0.70 eV Based on these above ΔG values, the last hydrogenation step is found to be the potential-determining step (PDS) for the ECOR to CH_4, having the maximum ΔG of 0.70 eV among all the elementary reaction steps, thus the corresponding U_L is predicted to be −0.70 V. As these double TM atoms anchored on C_9N_4 monolayers can serve as possible dual-active sites, we wonder besides the C_1 products, whether more valuable C_2 products can be produced through the ECOR on these $TM_2@C_9N_4$ systems. Therefore, we examine the potentiality of the ECOR toward C_2 products by firstly studying the performance for coinstantaneous adsorption of two CO molecules on our designed $TM_2@C_9N_4$ catalysts. As shown in Fig. 4a, both of the CO molecules are separately adsorbed on the top sites of TM atoms, forming the 2*CO species with two TM-C bonds, in which the distances between the two C atoms are in the range of 2.63 - 2.71 Å, while the TM-C bond lengths are 1.80 Å for $Fe_2@C_9N_4$, 1.72 Å for $Co_2@C_9N_4$, 1.73 Å for $Ni_2@C_9N_4$, and 1.79 Å for $Cu_2@C_9N_4$. The calculated adsorption energies of the 2*CO species on $TM_2@C_9N_4$ (TM = Fe, Co, Ni, and Cu) are found to be −2.94, −3.12, −2.99, and −2.30 eV, respectively. These results mean that the $TM_2@C_9N_4$ systems have sufficient capability to simultaneously capture both of the two CO molecules, which would be conducive to the subsequent CO coupling process.

Following the formation of two separately adsorbed *CO, we further study the extremely challenging process of the CO coupling on these $TM_2@C_9N_4$ catalysts, which is widely recognized as the

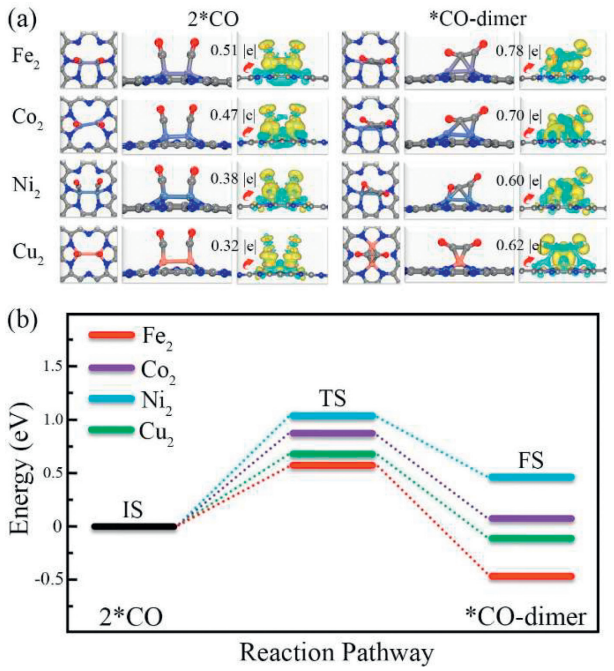

Fig. 4. (a) The optimized geometric structures and the corresponding charge density differences of 2*CO and *CO-dimer for the designed $TM_2@C_9N_4$ catalysts, where the isosurface values are set to 0.003 e/Å^3, and the yellow (cyan) region represents the charge accumulation (depletion). (b) The calculated relative energy changes of the reaction $2*CO \rightarrow *CO\text{-dimer}$.

vital step in the generation of C_2 products. Hence, based on the CI-NEB method, we compute the kinetic energy barrier to check whether the two chemisorbed *CO species can be successfully dimerized. It can be seen from Fig. 4b that our designed four catalysts exhibit favorable kinetics for the reaction $2*CO \rightarrow *CO\text{-dimer}$, since the transition state barriers are predicted to be 0.54 eV for $Fe_2@C_9N_4$, 0.83 eV for $Co_2@C_9N_4$, 1.08 eV for $Ni_2@C_9N_4$, and 0.64 eV for $Cu_2@C_9N_4$. And more notably, the obtained values are comparable to those of previous reported ECOR electrocatalysts, for instance, Cu+B@g-C_3N_4 (0.63 eV) [24], TM+*B*@BlackP (0.52 - 0.91 eV) [26], Cu_2@g-CN (1.16 eV) [29], Cu (211) surface (1.62 eV) [55], B@C_2N (0.73 eV) [56], Cu_2B_2 monolayer (0.41 eV)

[57], and $Cu_2Zn_2@C_5N_2H_2$ (0.4 eV) [58]. Moreover, the conversions of two CO molecules into the *CO-dimer on $TM_2@C_9N_4$ (TM = Fe, Co, Ni, and Cu) are highly exothermic by 3.41, 3.04, 2.54 and 1.56 eV, respectively. Furthermore, as shown in Fig. 4a, there appear new C–C bonds in the *CO-dimer with the lengths of 1.41 Å for $Fe_2@C_9N_4$, 1.40 Å for $Co_2@C_9N_4$, 1.40 Å for $Ni_2@C_9N_4$ and 1.36 Å for $Cu_2@C_9N_4$, which are shorter than not only the C–C distances in the 2*CO species but also that of ethane (1.54 Å). These observations provide further evidence for the high feasibility and stability of the *CO-dimer formed through CO coupling. Consequently, our designed $TM_2@C_9N_4$ catalysts demonstrate the impressive potential to facilitate the generation of C_2 products, highlighting their prospects in sustainable energy conversion and storage systems.

To gain a more comprehensive understanding of the CO coupling, we further calculate the charge density differences and the charge transfer of the 2*CO and *CO-dimer on the $TM_2@C_9N_4$ systems. As shown in Fig. 4a, there is apparent charge accumulation (yellow region) on the 2*CO, while the charge depletion (cyan region) occurs on the substrate. Bader charge analysis shows that 2*CO on $TM_2@C_9N_4$ (TM = Fe, Co, Ni, and Cu) catalysts gain 0.51 |e|, 0.47 |e|, 0.38 |e|, and 0.32 |e|, respectively. After forming the *CO-dimer *via* the CO coupling, we find that not only $TM_2@C_9N_4$ donate electrons to the *CO-dimer but also the *CO-dimer back-donate electrons to the $TM_2@C_9N_4$, and there is more significant charge transfer (about 0.78 |e|, 0.70 |e|, 0.60 |e|, and 0.62 |e|, respectively), implying the strong interaction between the *CO-dimer and $TM_2@C_9N_4$ catalysts. These results rationalize the high possibility of forming stable *CO-dimer on the $TM_2@C_9N_4$ systems, which would have a significant influence on the formation of multi-carbon products.

Next, we explore the energetically most favorable reaction pathway for the ECOR toward C_2 products on these $TM_2@C_9N_4$ systems, as illustrated by the free energy diagram in Fig. 5, in which the ΔG between any two elementary reaction steps along the reduction path has the least value. When the C_9N_4 monolayers anchored Fe_2, Co_2, and Ni_2 dual atoms, the CO molecule can be ultimately reduced to C_2H_5OH product through a successive protonation of *CO-dimer, which proceeds along the following pathway: $2CO(g) \rightarrow {}^*CO\text{-}dimer \rightarrow {}^*COCHO \rightarrow {}^*CHOCHO \rightarrow {}^*CHOCHOH \rightarrow {}^*CHOCH_2OH \rightarrow {}^*CH_2CHO \rightarrow {}^*CH_3CHO \rightarrow {}^*CH_3CH_2O \rightarrow {}^*CH_3CH_2OH$. It should be pointed out that the C_2H_5OH and C_2H_4 pathways differ at the step of $^*CH_2CHO$ hydrogenation, and their free energy changes are −0.19 *vs.* 0.20 eV for $Fe_2@C_9N_4$, −0.31 *vs.* 0.45 eV for $Co_2@C_9N_4$, and −0.23 *vs.* 0.67 eV for $Ni_2@C_9N_4$. Consequently, the C_2H_5OH pathway is followed. The PDS for all the $Fe_2@C_9N_4$, $Co_2@C_9N_4$, and $Ni_2@C_9N_4$ systems are the final protonation step of $^*CH_3CH_2O + (H^+ + e^-) \rightarrow {}^*CH_3CH_2OH$, which are uphill by 0.06, 0.26, and 0.31 eV in their free energy profiles, respectively. Thus, the corresponding U_L values are calculated to be −0.06, −0.26, and −0.31 V, respectively.

As for the $Cu_2@C_9N_4$ system, the first protonation of the adsorbed *CO-dimer is more inclined to generate *CO*COH and the C_2H_5OH and C_2H_4 pathways differ at the step of $^*CH_2CHOH$ hydrogenation with the free energy changes of −0.47 and 0.11 eV, respectively. Hence, the C_2H_4 product is more likely to be produced *via* subsequent continuous protonation plus reduction process. And the whole reaction path is as follows: $2CO(g) \rightarrow {}^*CO\text{-}dimer \rightarrow {}^*COCOH \rightarrow {}^*CCO \rightarrow {}^*CHCO \rightarrow {}^*CH_2CO \rightarrow {}^*CH_2CHO \rightarrow {}^*CH_2CHOH \rightarrow {}^*CH_2CH \rightarrow {}^*CH_2CH_2$. Based on the calculated reaction free energy diagram of the most favorable pathway, the PDS is identified to be $^*CHCO + (H^+ + e^-) \rightarrow {}^*CH_2CO$, and the whole ECOR process only demands an energy injection of 0.46 eV That is to say, the U_L for generating C_2H_4 product on $Cu_2@C_9N_4$ is −0.46 V.

Table 1
The computed limiting potentials and products of the designed $TM_2@C_9N_4$ along with other various 2D catalysts.

Catalysts	Limiting potentials and products
Ni+B@BlackP [26]	−0.28 V (C_2H_6)
B+P@C_2N [27]	−0.44 V (C_2H_4)
Cu_2@g-CN [29]	−0.47 V (C_2H_4)
Cu_2B_2 [57]	−0.59 V (C_2H_5OH)
$Cu_2Zn_2@C_5N_2H_2$ [58]	−0.46 V (C_2H_5OH)
Cu@$MoSi_2N_4$ [59]	−0.44 V (C_2H_6), −0.47 V (C_2H_5OH) and −0.47 V (C_2H_4)
This work	−0.06 ∼ −0.31V (C_2H_5OH) and −0.46 V (C_2H_4)

As discussed above, our proposed bimetallic $TM_2@C_9N_4$ systems have suitable U_L to achieve the electrochemical reduction of CO molecules into more valuable C_2 products, which are comparable with or even lower than those of the electrocatalysts reported in previous studies (Table 1), such as Ni+*B*@BlackP (−0.28 V for C_2H_6) [26], B + P@C_2N (−0.44 V for C_2H_4) [27], Cu_2@g-CN (−0.47 V for C_2H_4) [29], Cu_2B_2 (−0.59 V for C_2H_5OH) [57], $Cu_2Zn_2@C_5N_2H_2$ (−0.46 V for C_2H_5OH)[58], and Cu@$MoSi_2N_4$ (−0.44 V for C_2H_6, −0.47 V for C_2H_5OH and −0.47 V for C_2H_4) [59]. These observations suggest that our proposed four electrocatalysts would possess high ECOR activities for producing valuable C_2 products rather than C_1 products.

As is well known, the HER would compete with the ECOR as the major side reaction and result in low FE, once the $(H^+ + e^-)$ pairs are apt to participate in hydrogen evolution rather than CO reduction. In order to examine the ECOR selectivity, the hydrogen adsorption Gibbs free energy ($\Delta G_{^*H}$) of these $TM_2@C_9N_4$ systems are further investigated. As illustrated in Fig. 6a, the $\Delta G_{^*H}$ values of the $TM_2@C_9N_4$ systems are calculated to be −0.24, 0.46, −0.20, and −0.77 eV for TM = Fe, Co, Ni, and Cu, respectively, and thus the corresponding U_L required to initiate the HER are −0.24, −0.46, −0.20 and −0.77 V, respectively. Noted that the $\Delta G_{^*H}$ at other possible sites shown in Fig. S6 (Supporting information) have many positive values (Table S1 in Supporting information), indicating that the protons are unstably adsorbed. Furthermore, as shown in Fig. 6b, the differences between the U_L required for the ECOR and HER, *i.e.*, U_L(ECOR) - U_L(HER), are found to be 0.18 V for $Fe_2@C_9N_4$, 0.20 V for $Co_2@C_9N_4$, −0.11 V for $Ni_2@C_9N_4$, and 0.31 V for $Cu_2@C_9N_4$, indicating an excellent suppressing effect on HER during the ECOR process except for $Ni_2@C_9N_4$. These results suggest that the C_9N_4 monolayers anchored with Fe_2, Co_2 and Cu_2 dual atoms would possess great potential as ECOR electrocatalysts for C_2 products with both of superior catalytic activity and high selectivity.

In conclusion, we devise four kinds of C_9N_4 based bimetallic electrocatalysts, designated as $TM_2@C_9N_4$ (TM = Fe, Co, Ni, and Cu), and subsequently evaluate their potentialities of ECOR toward valuable C_1 and C_2 products through the extensive DFT calculations. Our calculations show that the synergy effect of transition-metal dual atoms anchored on C_9N_4 monolayers enables the two chemisorbed CO molecules to couple into the crucial *CO-dimer intermediates both thermodynamically and kinetically. Moreover, based on the Gibbs free energy diagrams, all these $TM_2@C_9N_4$ systems are identified to have high ECOR activities toward C_2 products rather than C_1 products. C_2H_5OH formation is preferred on the $Fe_2@C_9N_4$, $Co_2@C_9N_4$, and $Ni_2@C_9N_4$ systems with rather low U_L of −0.06, −0.26, and −0.31 V, respectively, while the $Cu_2@C_9N_4$ system can catalyze the conversion of CO for C_2H_4 product with the U_L of −0.46 V. Meanwhile, these proposed $TM_2@C_9N_4$ electrocatalysts show well-suppressed HER ability except for $Ni_2@C_9N_4$, indicating the excellent selectivity for C_2 products. These findings not only accelerate the discovery of effective ECOR electrocatalysts for more valuable multi-carbon products but also contribute to developing C_9N_4-based DACs in the future.

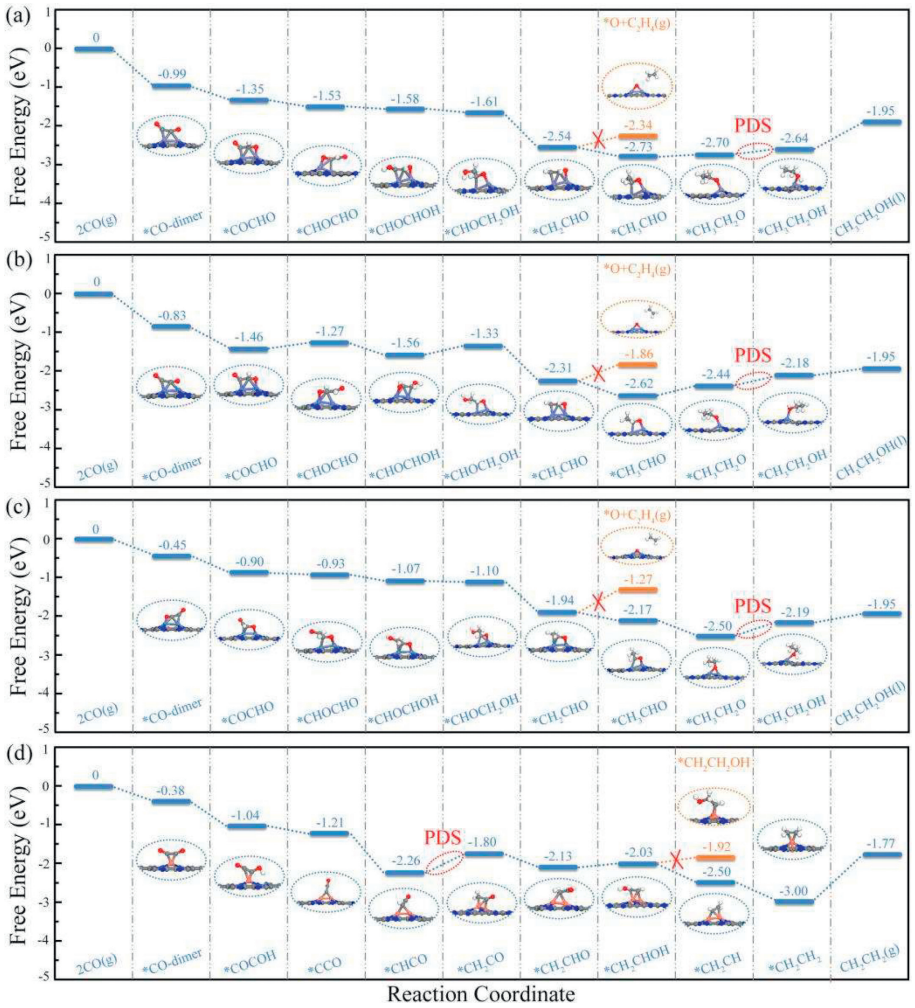

Fig. 5. Computed Gibbs free energy diagrams for the ECOR toward C_2 products on (a) $Fe_2@C_9N_4$, (b) $Co_2@C_9N_4$, (c) $Ni_2@C_9N_4$, and (d) $Cu_2@C_9N_4$ along the most energetically favorable pathway. The insets give the optimized structures of each reaction intermediates.

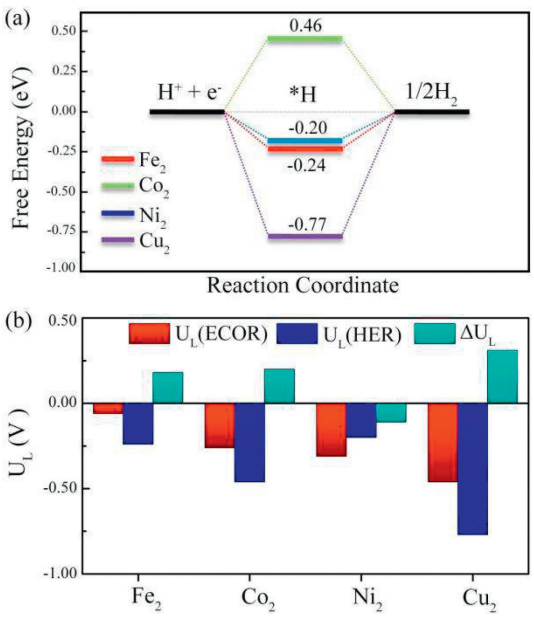

Fig. 6. Free energy diagrams of HER on the $TM_2@C_9N_4$ systems. (b) Limiting potentials for the ECOR U_L(ECOR), U_L(HER), and the differences (ΔU_L) between them on the $TM_2@C_9N_4$ systems.

Declaration of competing interest

The authors declare that they have no known competing financial interests or personal relationships that could have appeared to influence the work reported in this paper.

Acknowledgments

This work was supported by the Science and Technology Research Project of Hubei Provincial Department of Education (No. D20212603), Hubei University of Arts and Science (No. 2020kypytd002), National Natural Science Foundation of China (No. 22303098) and Natural Science Foundation of Hubei Province (No. 2022CFC030).

Supplementary materials

Supplementary material associated with this article can be found, in the online version, at doi:10.1016/j.cclet.2023.109050.

References

[1] M. Jouny, G.S. Hutchings, F. Jiao, Nat. Catal. 2 (2019) 1062–1070.
[2] W. Ma, X. He, W. Wang, et al., Chem. Soc. Rev. 50 (2021) 12897–12914.
[3] H. Du, J. Fu, L.X. Liu, et al., Mater. Today 59 (2022) 182–199.
[4] H. Yang, S. Li, Q. Xu, Chin. J. Catal. 48 (2023) 32–65.
[5] S. Jin, Z. Hao, K. Zhang, et al., Angew. Chem. Int. Ed. 60 (2021) 20627–20648.

[6] J. Gao, A. Bahmanpour, O. Kröcher, et al., Nat. Chem. 15 (2023) 705–713.
[7] T. Liu, Y. Wang, Y. Li, JACS Au 3 (2023) 943–952.
[8] Y. Ji, Z. Chen, R. Wei, et al., Nat. Catal. 5 (2022) 251–258.
[9] J. Li, H. Xiong, X. Liu, et al., Nat. Commun. 14 (2023) 698.
[10] T. He, G. Kour, X. Mao, et al., J. Catal. 382 (2020) 49–56.
[11] L. Wang, D.C. Higgins, Y. Ji, et al., Proc. Natl. Acad. Sci. 117 (2020) 12572–12575.
[12] X. Yan, M. Zhang, Y. Chen, et al., Angew. Chem. Int. Ed. 62 (2023) e202301507.
[13] X.F. Yang, A. Wang, B. Qiao, et al., Acc. Chem. Res. 46 (2013) 1740–1748.
[14] J. Zhao, Z. Chen, J. Zhao, et al., Appl. Surf. Sci. 498 (2019) 143868.
[15] H. Bao, Y. Qiu, X. Peng, et al., Nat. Commun. 12 (2021) 238.
[16] W. Wang, Y. Gao, H. Li, et al., Appl. Surf. Sci. 545 (2021) 148953.
[17] Y. Yang, R. Song, X. Fan, et al., Chin. Chem. Lett. 34 (2023) 107257.
[18] Y. Ouyang, L. Shi, X. Bai, et al., Chem. Sci. 11 (2020) 1807–1813.
[19] T. Cheng, H. Xiao, W.A. Goddard, Proc. Natl. Acad. Sci. 114 (2017) 1795–1800.
[20] C. Zhu, C. Wang, M. Zhang, et al., ACS Appl. Mater. Interfaces 13 (2021) 3845–3855.
[21] H. Xiao, T. Cheng, W.A. Goddard, J. Am. Chem. Soc. 139 (2017) 130–136.
[22] S. Li, A. Guan, C. Yang, et al., ACS Mater. Lett. 3 (2021) 1729–1737.
[23] W. Rong, H. Zou, S. Tan, et al., CCS Chem. 5 (2023) 1176–1188.
[24] T. He, K. Reuter, A. Du, J. Mater. Chem. A 8 (2020) 599–606.
[25] Y. Meng, S.B. Cheng, Z. Wu, Appl. Surf. Sci. 597 (2022) 153761.
[26] L. Kong, Z. Chen, Q. Cai, et al., Chin. Chem. Lett. 33 (2022) 2183–2187.
[27] H. Wang, G. Ren, Y. Zhao, et al., J. Mater. Chem. A 10 (2022) 4703–4710.
[28] Y.Q. Liu, Z.Y. Guo, Z.Y. Qiu, et al., ACS Appl. Mater. Interfaces 14 (2022) 46657–46664.
[29] Y. Li, Y. Qian, Y. Ji, et al., J. Mater. Chem. A 7 (2019) 24000–24004.
[30] L. Tan, C. Nie, Z. Ao, et al., J. Mater. Chem. A 9 (2021) 17–33.
[31] W. Wang, J. Meng, Y. Hu, et al., J. Mater. Chem. A 10 (2022) 9848–9857.
[32] L. Zhao, Y. Li, G. Zhou, et al., Chin. Chem. Lett. 32 (2021) 900–905.
[33] S. Li, M. Shi, J. Yu, et al., Chin. Chem. Lett. 32 (2021) 1977–1982.
[34] Q. Gao, L. Zhang, C. Zheng, et al., Chin. Chem. Lett. 33 (2022) 3941–3946.
[35] H. Chen, S. Zhang, W. Jiang, et al., J. Mater. Chem. A 6 (2018) 11252–11259.
[36] Y. Zhou, G. Gao, J. Kang, et al., Nanoscale 11 (2019) 18169–18175.
[37] Z. Xue, X. Zhang, J. Qin, et al., Nano Energy 80 (2021) 105527.
[38] B. He, J. Shen, Z. Lu, et al., Appl. Surf. Sci. 527 (2020) 146828.
[39] J. Sun, P. Xia, Y. Lin, et al., Nanoscale Horiz. 8 (2023) 211–223.
[40] G. Kresse, J. Furthmuller, Phys. Rev. B 54 (1996) 11169.
[41] P.E. Blöchl, Phys. Rev. B 50 (1994) 17953.
[42] J.P. Perdew, K. Burke, M. Ernzerhof, Phys. Rev. Lett. 77 (1996) 3865.
[43] S. Grimme, J. Comput. Chem. 27 (2006) 1787–1799.
[44] H.J. Monkhorst, J.D. Pack, Phys. Rev. B 13 (1976) 5188.
[45] G. Henkelman, B.P. Uberuaga, H. Jonsson, J. Chem. Phys. 113 (2000) 9901–9904.
[46] Z. Xue, X. Zhang, J. Qin, et al., J. Energy Chem. 57 (2021) 443–450.
[47] J. Huang, C. Zhou, Z. Chu, et al., Phys. Chem. Chem. Phys. 23 (2021) 1868–1873.
[48] J. Wang, M. Shi, G. Yi, et al., Mol. Catal. 511 (2021) 111726.
[49] S. Wang, L. Shi, X. Bai, et al., ACS Cent. Sci. 6 (2020) 1762–1771.
[50] X. Lv, W. Wei, B. Huang, et al., Nano Lett. 21 (2021) 1871–1878.
[51] J. Wang, M. Shi, G. Yi, et al., Chin. Chem. Lett. 33 (2022) 4623–4627.
[52] H. Liu, Q. Huang, W. An, et al., J. Energy Chem. 61 (2021) 507–516.
[53] Y. Zang, Q. Wu, S. Wang, et al., J. Phys. Chem. Lett. 13 (2022) 527–535.
[54] Y. Sun, S. Wang, J. Jia, et al., J. Mater. Chem. A 10 (2022) 14460–14469.
[55] J.H. Montoya, A.A. Peterson, J.K. Nørskov, ChemCatChem 5 (2013) 737–742.
[56] Z. Chen, J. Zhao, J. Zhao, et al., Nanoscale 11 (2019) 20777–20784.
[57] J. Jia, H. Zhang, Z. Wang, et al., J. Mater. Chem. A 8 (2020) 9607–9615.
[58] D. Zhang, O.V. Prezhdo, L. Xu, J. Am. Chem. Soc. 145 (2023) 7030–7039.
[59] Y. Linghu, T. Tong, C. Wu, Appl. Surf. Sci. 609 (2023) 155332.